

<https://doi.org/10.1038/s42004-024-01129-y>

# A unified view on enzyme catalysis by cryo-EM study of a DNA topoisomerase

Check for updates

Chiung-Wen Mary Chang<sup>1,3</sup>, Shun-Chang Wang<sup>1</sup>, Chun-Hsiung Wang<sup>1</sup>, Allan H. Pang<sup>1,4</sup>,  
Cheng-Han Yang<sup>1</sup>, Yao-Kai Chang<sup>1</sup>, Wen-Jin Wu<sup>1</sup> & Ming-Daw Tsai<sup>1,2</sup> ✉

The theories for substrate recognition in enzyme catalysis have evolved from lock-key to induced fit, then conformational selection, and conformational selection followed by induced fit. However, the prevalence and consensus of these theories require further examination. Here we use cryogenic electron microscopy and African swine fever virus type 2 topoisomerase (*AsfvTop2*) to demonstrate substrate binding theories in a joint and ordered manner: catalytic selection by the enzyme, conformational selection by the substrates, then induced fit. The *apo-AsfvTop2* pre-exists in six conformers that comply with the two-gate mechanism directing DNA passage and release in the Top2 catalytic cycle. The structures of *AsfvTop2*-DNA-inhibitor complexes show that substantial induced-fit changes occur locally from the closed *apo*-conformer that however is too far-fetched for the open *apo*-conformer. Furthermore, the ATPase domain of *AsfvTop2* in the MgAMP-PNP-bound crystal structures coexist in reduced and oxidized forms involving a disulfide bond, which can regulate the *AsfvTop2* function.

The past half century has seen major advancements in the theories for substrate recognition in enzyme catalysis from lock-key<sup>1</sup> to induced fit<sup>2</sup>, then conformational selection<sup>3–5</sup>, and recently conformational selection followed by induced fit<sup>4,6,7</sup>. Furthermore, the *apo*-enzyme (ligand-free) was suggested to pre-exist as a subset of catalytically relevant conformers (termed catalytic selection here) for facilitating the conformational selection<sup>7–9</sup>. The concept of conformational selection started from the early report of multiple conformational states of myoglobin<sup>10</sup> to the recent emphasis of conformational landscapes and conformational selection<sup>4,6,7,11–16</sup>. Of particular interest is the finding by Kern and coworkers that, even in the absence of ligands, adenylate kinase (Adk) in crystals pre-exists in three conformers with varying degrees of lid openness along the catalytic trajectory, suggesting that the structure of the *apo* enzyme has evolved to adopt conformations ready to bind its substrates and reaction intermediates<sup>8</sup>, a property termed catalytic selection herein. A recent study showed that this property is coupled with the conformational selection and induced fit mechanisms upon ligand binding, based on an advanced nuclear magnetic resonance (NMR) relaxation approach that enabled the structure determination of Adk at high-energy and minor populated states<sup>7</sup>. Related properties were also found in several other proteins<sup>17</sup>, though Adk has been most extensively investigated. In fact, the catalytic selection mechanism could be widespread, but only one structure is solved a time. For example, in the *apo* state of the

four members of the X-family DNA polymerases, Pol  $\beta$  exists in an open form<sup>18</sup> while Pol  $\lambda$ <sup>19</sup>, Pol  $\mu$ <sup>20</sup> and TdT<sup>21</sup> pre-exist in the closed form.

On the other hand, the relationship between protein dynamics and functions was often examined for relatively small monomeric proteins by NMR primarily, as in the signaling protein NtrC<sup>22</sup>, dihydrofolate reductase (DHFR)<sup>11</sup> and tyrosine phosphatases<sup>12</sup>. The Adk study used X-ray crystallography, NMR, and MD simulation<sup>7,8,23</sup>, which well encapsulated the subtle yet significant local differences between the conformational sub-states. However, for these theories to be broadly applicable, they need to be demonstrated for large and multimeric enzymes that catalyze complicated reactions. The enzyme used in this study is a type II DNA topoisomerase (Top2) from African swine fever virus (*Asfv*), a dimeric multi-subdomain enzyme (271 kDa) that catalyzes multistep reactions to modulate DNA topology (Fig. 1).

It is now common to identify multiple structures from a single dataset in cryogenic-electron microscopy (cryo-EM)<sup>24,25</sup>. A vast majority of such conformers involve different ligand binding states or reaction intermediates. Only limited examples were found to address conformational variations in an *apo* enzyme<sup>26–30</sup>. In this work, we use cryo-EM to evaluate the current catalytic theories with *AsfvTop2* and examine its induced fit conformational changes upon binding of ligands. The results allow us to propose a three-stage mechanism that encapsulates the substrate binding theories in a joint

<sup>1</sup>Institute of Biological Chemistry, Academia Sinica, Taipei 115, Taiwan. <sup>2</sup>Institute of Biochemical Sciences, National Taiwan University, Taipei 106, Taiwan.

<sup>3</sup>Present address: Institute of Biochemistry and Molecular Biology, China Medical University, Taichung, Taiwan. <sup>4</sup>Present address: Department of Biological Sciences, National University of Singapore, Singapore, Singapore. ✉e-mail: [mchtsai@gate.sinica.edu.tw](mailto:mchtsai@gate.sinica.edu.tw)



**Table 1 | Summary of key structural information**

Sample no.	Structure name	MgAMP-PNP	DNA	Inhibitor	Conf no.	DNAgate	C-gate	Resoln (Å)	PDB code	EMDB code
X-ray crystallography of <i>Asfv</i> Top2 ATPase domain										
1	ATPase-red	+	-	-	-	-	-	1.73	8JA2	-
2	ATPase-ox	+	-	-	-	-	-	1.14	8JA1	-
Cryo-EM structures of full-length <i>Asfv</i> Top2										
3	<i>Apo-Asfv</i> Top2	-	-	-	Ia	more open	closed	3.42	8J87	EMD-36062
					Ib	open	closed	3.49	8J88	EMD-36063
					IIa	closed	closed	2.31	8J89	EMD-36064
					IIb	closed	closed	2.51	8J8A	EMD-36065
					IIIa	closed	more open	2.43	8J8B	EMD-36066
					IIIb	closed	open	2.69	8J8C	EMD-36067
Cryo-EM reconstruction of cleavage core domain with DNA/drug bound										
4	EDI-1	+	Cut02a	etoposide	II	closed	closed	2.70	8J9V	EMD-36116
5	EDI-2	+	Cut02b	etoposide	II	closed	closed	2.74	8J9W	EMD-36117
6	EDI-3	+	Cut02a	<i>m</i> -AMSA	II	closed	closed	3.0	8J9X	EMD-36118
Cryo-EM reconstruction of entire <i>Asfv</i> Top2 with DNA/drug bound										
4	full complex	+	Cut02a	etoposide	II	closed	closed	3.68	-	EMD-36473

The formal PDB validation reports of all deposited structures and maps are provided in Supplementary Data 7–18.

The distribution of the three primary *apo*-conformers is approximately 1:4:2 (Supplementary Fig. 1b). Even though such differences are modest energetically, they do suggest that the closed state II is the most stable state, followed by the C-gate open state III and then the open state I. These thermodynamic properties are reflected in their structural properties described in the following sections.

### Catalytic selection of *apo-Asfv*Top2

Global conformational changes between different conformational states are illustrated by overlaying the conformers Ia/IIa, Ia/IIIa, and IIa/IIIa (Fig. 2c). The changes in the Ia/IIa pair are mainly in the closing of the DNA-gate via the WHD subdomain. The major difference between IIa and IIIa is hinge-like movements of the coiled-coils ( $\alpha 22$  and  $\alpha 27$ ) with approximately 13.6° and 18.3° tilts, respectively, governing the mobile states of the C-gate (Fig. 2c). The key determinants of the movements likely involve the flexible turn (residues 1158–1167) connecting the helices  $\alpha 27$  and  $\alpha 28$ . Of which, two proline residues (P1163/P1165) provide certain degree of flexibility<sup>61</sup> to this joint region, which was previously defined as an elbow<sup>46</sup>. Additionally, the indole ring side chain of W1170 from *apo*-IIIa turns clockwise with the nitrogen atom of its pyrrole ring shifted away from the hydroxyl group of Y1043. The interaction between the two aromatic residues is weakened in the *apo*-IIIa, therefore the helix  $\alpha 22$  is less engaged with the helix  $\alpha 28$  and attains flexibility to introduce the swing motion at the coiled-coil region. The continuum of structural conversion from conformers Ia to IIIb is shown in Supplementary Movie 2 (Structure conversion of *apo-Asfv*Top2 conformers), which not only highlights the inherent dynamic nature of *apo*-Top2s, but also illustrates the unexpected yet functionally relevant conformational changes reminiscent of the process for the unidirectional strand passage in the Top2 catalytic cycle (Fig. 1b)<sup>46,59,62,63</sup>.

To further provide the structural basis and functional relevance, we compared the conformers from the *apo* form of *Asfv*Top2 with individual structures of the cleavage core domain of yeast Top2, where each structure was solved separately under different conditions. As shown in Fig. 2d, conformers Ia/Ib were aligned globally with two *apo*-yeast Top2 structures<sup>45,46</sup>. Subsequently, the TOPRIM subdomain is posited downwards for constituting the DNA binding groove, as shown by aligning conformer IIa and the DNA bound structure of yeast Top2 (pdb 3l4k<sup>64</sup>, closed form). Furthermore, conformer IIIa resembles the C-gate open structure of yeast Top2 (pdb 2rgr<sup>48</sup>), one of the key conformations for DNA

strand transport<sup>48,59</sup>. The parallel conformational changes between *Asfv* IIa-to-IIIa in the absence of DNA and yeast 3l4k<sup>64</sup>-to-2rgr<sup>48</sup> in the presence of DNA provide strong support for the catalytic selection mechanism of *Asfv*Top2.

### Conformational selection by ligands

In the conventional concept, the structural change between the *apo* form (yeast Top2 structure 1bgw<sup>45</sup> or 1bjt<sup>46</sup>) and the DNA complex (2rgr<sup>48</sup> or 3l4k<sup>64</sup>) can be attributed to induced fit, as has been addressed for 1bgw<sup>45</sup> and 2rgr<sup>48</sup> previously. However, it has not been addressed how DNA is able to bind a wide-open structure and induce large conformational changes, both globally and locally. Since the *apo*-state can pre-exist in multiple conformational states, the ligands are expected to select a conformer that is competent for ligand binding, according to the conformational selection theory<sup>3–5</sup>. Comparison with yeast Top2 structures suggested that the DNA complexes resemble *apo-Asfv*Top2 conformers II or III (*apo*-II or *apo*-III, respectively, Fig. 2d).

To obtain direct evidence for conformational selection, we performed structural analyses of *Asfv*Top2 complexes with DNA and an inhibitor. The sequences of DNA for the structural study are shown in Fig. 3a (Cut02a and Cut02b), which were chosen based on the DNA cleavage specificity of the active full-length *Asfv*Top2 (Supplementary Fig. 7) and described in Supplementary Note 1, Supplementary Fig. 8, and Supplementary Tables 1–3. Then we solved the cryo-EM structures of the full-length *Asfv*Top2 complexed with MgAMP-PNP (adenyl-*im*idodiphosphate, a non-hydrolysable ATP analogue), DNA, and the Top2-targeting drug etoposide (a podophyllotoxin, with both Cut02a and Cut02b) (enzyme-DNA-inhibitor complexes EDI-1 and EDI-2, respectively) or *m*-AMSA (an aminoacridine, with Cut02a) (EDI-3) (2.70–3.0 Å, Tables 1 and 3) to dissect the specific binding of the DNA segments to the enzyme. Both etoposide and *m*-AMSA have been approved as anti-cancer drugs for human<sup>65</sup>, and have been shown to decrease the DNA decatenation activity of *Asfv*Top2 in vitro<sup>35</sup>.

The global structures of all three complexes resemble that of *apo*-II. As an example, the 3D maps of the complex with etoposide and Cut02a DNA (EDI-1) and those of the bound DNA and inhibitor are shown in Fig. 3b. The corresponding maps for EDI-2 and EDI-3 are shown in Supplementary Figs. 3 and 4, respectively. In all three structures, the DNA segment adopts a U-shaped conformation positioned on the DNA binding surface

**Table 2 | The statistics of cryo-EM data collection, structure refinement, and validation for the apo-AsfvTop2 structure in three states, containing six conformers**

<i>apo-AsfvTop2</i>						
Data collection and processing						
Micrographs	8900					
Magnification	105,000					
Voltage (kV)	300					
Electron exposure (e <sup>-</sup> /Å <sup>2</sup> )	50					
Defocus range (μm)	-1.5 --2.5					
Pixel size (Å)	0.83					
Symmetry imposed	C2					
Initial particle images (no.)	3,260,785					
Conformer	Ia	Ib	IIa	IIb	IIIa	IIIb
PDB/EMDB code	8J87/EMD-36062	8J88/EMD-36063	8J89/EMD-36064	8J8A/EMD-36065	8J8B/EMD-36066	8J8C/EMD-36067
Final particle images (no.)	79,500	75,839	567,069	393,995	341,283	180,474
Map resolution (Å)	3.42	3.49	2.31	2.51	2.43	2.69
FSC threshold	0.143	0.143	0.143	0.143	0.143	0.143
Map resolution range (Å)	3.0–15.0	3.0–15.0	2.0–8.0	2.0–9.0	2.0–8.0	2.0–10.0
Refinement						
Initial model used (PDB code)	1ZVU <sup>47</sup>	Ia(8J87)	Robetta prediction <sup>81</sup>	IIa(8J89)	IIa(8J89)	IIIa(8J8B)
Model resolution (Å)	3.42	3.49	2.31	2.51	2.43	2.69
Model resolution range (Å)	3.0–15.0	3.0–15.0	2.0–8.0	2.0–9.0	2.0–8.0	2.0–10.0
Map sharpening B factor (Å <sup>2</sup> )	-96.5	-111.5	-80.8	-86.7	-79.7	-79.7
Model composition						
Protein residues	954	954	1502	1502	1518	1434
Non-hydrogen atoms	7846	7846	12,222	12,222	12,330	11,650
Ligand	0	0	0	0	0	0
B factors (Å <sup>2</sup> )						
Protein	157.69	194.85	96.39	110.18	109.82	104.39
R.m.s. deviations						
Bond lengths (Å)	0.002	0.002	0.002	0.003	0.002	0.002
Bond angles (°)	0.562	0.562	0.457	0.498	0.432	0.432
Validation						
MolProbity score	1.66	1.64	1.56	1.41	1.50	1.54
Clash score	7.20	5.61	5.77	7.45	5.43	4.89
Poor rotamers (%)	0.00	0.00	0.00	0.00	0.00	0.00
Ramachandran plot (%)						
Favored	96.11	95.16	96.39	97.99	96.49	95.91
Allowed	3.89	4.84	3.61	2.01	3.51	4.09
Disallowed	0.0	0.0	0.00	0.00	0.00	0.00

constituted of the TOPRIM, WHD, and Tower subdomains from both subunits (Fig. 3c). Importantly, despite the global similarity to apo-II by comparison Figs. 3c and Fig. 2b, there are substantial local changes as a result of induced fit. In the next two sections we first address the unique features of the AsfvTop2-DNA-inhibitor complexes relative to Top2s from other organisms, and then the induced fit conformational changes in the AsfvTop2.

### Uniqueness of AsfvTop2-DNA-drug complex

Specific enzyme-DNA interactions in the three complexes are shown by schematic diagrams (Supplementary Fig. 9). In comparison with the corresponding diagram for eukaryotic Top2<sup>48,66</sup>, the conserved DNA-intercalating residue (I872 in human or I833 in yeast Top2) is replaced by the P852 in AsfvTop2 (Supplementary Fig. 5b). The well-conserved

isoleucine across eukaryotic and bacterial Top2s is involved in the DNA bending, and DNA-stimulated ATPase activity<sup>48,67</sup>. The alteration of the isoleucine to a proline by site-specific mutagenesis has been shown to dampen the *E. coli* Top2 (Top IV) functions in DNA bending and thus reduce ATPase activity<sup>47</sup>. Figure 3d shows that P852 and the conserved isoleucine from other Top2s residing at the β-hairpin loop (annotated as β-HP1 hereafter), protrude into DNA to different extents. The five-membered ring structure of P852 is intercalated between the DNA bases by an average distance of 4.0 Å (Fig. 3e). The β-HP1 is buttressed by another two β-HPs, and linked to the catalytic Y800 at the DNA-gate and helix α17 adjacent to the elbow (Fig. 3f). The potential functional relevance of this structural organization is elaborated in the following section. Additionally, AsfvTop2 lacks the essential conserved basic residue (K700 in yeast Top2) from the WHD subdomain (Supplementary Fig. 5b) for stabilizing the bent DNA

**Table 3 | The statistics of cryo-EM data collection, structure refinement, and validation for *AsfvTop2*/DNA/inhibitor structures (EDI-1, -2, -3) and the reconstruction of the full EDI-1 complex**

	<i>AsfvTop2</i> :Cut02aDNA:etoposide (EDI-1)		<i>AsfvTop2</i> :Cut02bDNA:etoposide (EDI-2)	<i>AsfvTop2</i> :Cut02aDNA: <i>m</i> -AMSA (EDI-3)
Data collection and processing				
Micrographs	11786		10919	9846
Magnification	105,000		105,000	105,000
Voltage (kV)	300		300	300
Electron exposure (e <sup>-</sup> /Å <sup>2</sup> )	50		42	42
Defocus range (μm)	-1.5 ~ -2.5		-1.5 ~ -2.5	-1.5 ~ -2.5
Pixel size (Å)	0.83		0.83	0.83
Reconstructions	Full complex	DNA binding/ cleavage domain	DNA binding/ cleavage domain	DNA binding/ cleavage domain
Symmetry imposed	C1	C2	C2	C2
Initial particle images (no.)	632,007		5,665,983	5,465,423
Final particle images (no.)	80,745		650,266	351,979
EMDB accession code	EMD-36473		EMD-36117	EMD-36118
PDB accession code	-		8J9W	8J9X
Map resolution (Å)	3.68		2.74	3.0
FSC threshold	0.143		0.143	0.413
Map resolution range (Å)	3.0-7.0		2.74-7.5	3.0-8.0
Refinement				
Initial model used (PDB code)	Ila(8J89)/6ZY7 <sup>69</sup>		EDI-1(8J9V)	EDI-1(8J9V)
Model resolution (Å)	2.70		2.74	3.0
Model resolution range (Å)	2.70-7.5		2.74-7.5	3.0-8.0
Map sharpening <i>B</i> factor (Å <sup>2</sup> )	-116.5		-116.2	-144.9
Model composition				
Non-hydrogen atoms	13,918		13,859	13,890
Protein residues	1556		1550	1556
Ligands	Etoposide:2 nucleotide:60 Mg <sup>2+</sup> :2		Etoposide:2 nucleotide:60 Mg <sup>2+</sup> :2	<i>m</i> -AMSA:2 nucleotide:60 Mg <sup>2+</sup> :2
<i>B</i> factors (Å <sup>2</sup> )				
Protein	135.86		145.02	164.51
Nucleotide	159.88		178.38	213.38
Ligand	127.46		170.85	171.42
R.m.s. deviations				
Bond lengths (Å)	0.003		0.004	0.003
Bond angles (°)	0.551		0.797	0.743
Validation				
MolProbity score	1.80		1.89	1.77
Clashscore	8.0		8.0	10.0
Poor rotamers (%)	0.00		0.00	0.00
Ramachandran plot				
Favored (%)	95.49		93.86	94.59
Allowed (%)	4.51		6.14	5.41
Disallowed (%)	0.00		0.00	0.00

conformation<sup>48</sup>. These distinct structural features likely differentiate the DNA modulation functions of *AsfvTop2* from other Top2s.

Binding of the two Top2-targeting drugs etoposide and *m*-AMSA to *AsfvTop2* is described in detail in Supplementary Note 2 and Supplementary Fig. 10. Structural comparison with human Top2-DNA-drug complexes<sup>66,68</sup> highlights the distinctive residues from the two species facilitating the drug binding in different modes. For instances, *AsfvTop2* lacks the conserved segment (PLR<sub>503</sub>GKXL) and polar residues that are characterized in its eukaryotic counterparts for the major interactions with the etoposide and *m*-AMSA, respectively (Fig. 3g, h). Based on the structural information,

general guidelines for drug design targeting *AsfvTop2* are summarized here: (1) a polycyclic aromatic core to assist drug intercalation into the DNA cleavage site as suggested for human Top2 targeting drug development<sup>68</sup>; (2) attaching a polar and bulky minor groove protruding moiety to the aromatic core that enhances the drug's binding and specificity towards the minor groove-binding pocket of *AsfvTop2*.

#### Induced fit from *apo*-Ila to EDI complex

By overlaying the *apo*-conformer Ila and the DNA/inhibitor bound *AsfvTop2* structure, Fig. 4a shows that the protein conformations of the two



**Table 4 | The statistics of X-ray structure data collection, processing and structure refinement and validation of *Asfv*-Top2 ATPase/MgAMP-PNP in reduced and oxidized states**

	Reduced	Oxidized
PDB code	8JA2	8JA1
Data Collection		
Space group	P6 <sub>1</sub> 22	P6 <sub>1</sub> 22
Unit cell dimensions		
a, b, c (Å)	85.92, 85.92, 212.01	85.76, 85.76, 212.30
α, β, γ (°)	90, 90, 120	90.00, 90.00, 120.00
Resolution (Å)	43.21–1.73 (1.82–1.73) <sup>a</sup>	43.18–1.14 (1.20–1.14) <sup>a</sup>
R <sub>merge</sub>	0.069 (0.404) <sup>a</sup>	0.098 (1.210) <sup>a</sup>
I/σI	18.6 (4.9) <sup>a</sup>	15.1 (2.1) <sup>a</sup>
Completeness (%)	99.0 (98.7) <sup>a</sup>	99.8 (98.6) <sup>a</sup>
Multiplicity	8.6 (8.4) <sup>a</sup>	20.1(13.2) <sup>a</sup>
Total reflections / Unique reflections	417449 (58802) <sup>a</sup> / 48808 (6982) <sup>a</sup>	3356924 (312727) <sup>a</sup> / 166668 (23634) <sup>a</sup>
CC <sub>1/2</sub>	0.999 (0.934) <sup>a</sup>	0.999 (0.696) <sup>a</sup>
Search model (PDB)	1PVG <sup>55</sup>	Reduced form (8JA2)
Structure refinement statistics		
R <sub>work</sub> /R <sub>free</sub>	0.1979 / 0.2163	0.1838 / 0.1870
No. of atoms		
Protein	3099	3078
AMP-PNP/Mg <sup>2+</sup>	31 / 1	31 / 1
Water	227	352
B-factors (Å <sup>2</sup> ) <sup>b</sup>		
Protein	21.4	21.23
AMP-PNP/Mg <sup>2+</sup>	12.3 / 12.6	9.0 / 7.4
Water	25.5	21.5
r.m.s. deviations		
Bond lengths (Å)	0.05	0.007
Bond angles (°)	1.703	1.037
Ramachandran plot (%) <sup>c</sup>		
favoured region	98.17	97.61
allowed region	1.83	2.39
disallowed region	0	0

<sup>a</sup>Numbers in parenthesis indicate the values in the highest resolution shell.

<sup>b</sup>Average B-factor calculated using the average B script in PyMOL Molecular Graphic System (Version 2.2.2).

<sup>c</sup>Ramachandran statistics generated from Phenix v.1.19<sup>82</sup>.

structures are very similar except that binding of DNA/inhibitor causes small subdomain reorientations to constitute the protein-DNA interface and re-organize the dimer interfaces at DNA- and C-gates (Fig. 4a and Supplementary Movie 3: DNA-induced subdomain reorientation of *Asfv*-Top2), which can be considered the induced fit by ligand binding to the pre-selected conformer IIa. Presumably, conformer IIb should work equally well due to its similarity to IIa.

Furthermore, comparison of the DNA-bound complex with the *apo*-*Asfv*-Top2 conformers unravels a flexible extended loop (from residue 481–493) protruding from the TOPRIM subdomain that becomes visible upon DNA binding (Fig. 4b). Sequence alignment (Supplementary Fig. 5b) indicates that this long-extended loop is unique for *Asfv*-Top2. As it resides at the vicinity of the DNA binding groove, and located opposite to the β-HP1 across the DNA (Fig. 4c), it could be involved in DNA modulation, analogous to the potential role of the human Top2 CTD (missing in *Asfv*-Top2)

in facilitating strand passage process<sup>69</sup>. Figure 4d highlights the differences in the protein-DNA specific interactions in that region between the viral and eukaryotic Top2-DNA complexes. The key positively charged residues involved in the DNA binding are well conserved amongst *Asfv* orthologues (Supplementary Fig. 11), which likely illustrates the conserved functionality of the DNA responsive loop in *Asfv*-Top2.

Another induced fit feature involves re-positioning of β-HP1 and subsequent movements of the neighboring structural elements that likely harbor functional relevance. Aligning EDI-1 and conformer IIa (Fig. 4e left panels) indicates that β-HP1 shifts downward in EDI-1, resulting in relocation of P852 by 8.3 Å to accommodate DNA binding. Simultaneously, several hydrophobic contacts are formed between β-HP1 and β-HP2, shifting the β-HP2 downward to form hydrophobic interactions with β-HP3 and helix α22 (Fig. 4e lower panels left and center), part of the coiled-coil C-gate region. The β-HP3 residing beneath the β-HP2 moves downward by 5.5 Å. Since the N-terminal end of β-HP3 is linked to the catalytic residue Y800 through a long β-strand linker and two small α-helices (Figs. 3f and 4e lower right), the spatial location of the Y800 in EDI-1 is shifted from *apo*-IIa by a distance of 7.3 Å and moves upward toward DNA. These DNA-responsive conformational changes occurring in the DNA binding groove are relayed to the active site and potentially the C-gate region, which likely collectively coordinate the dynamic gating operation.

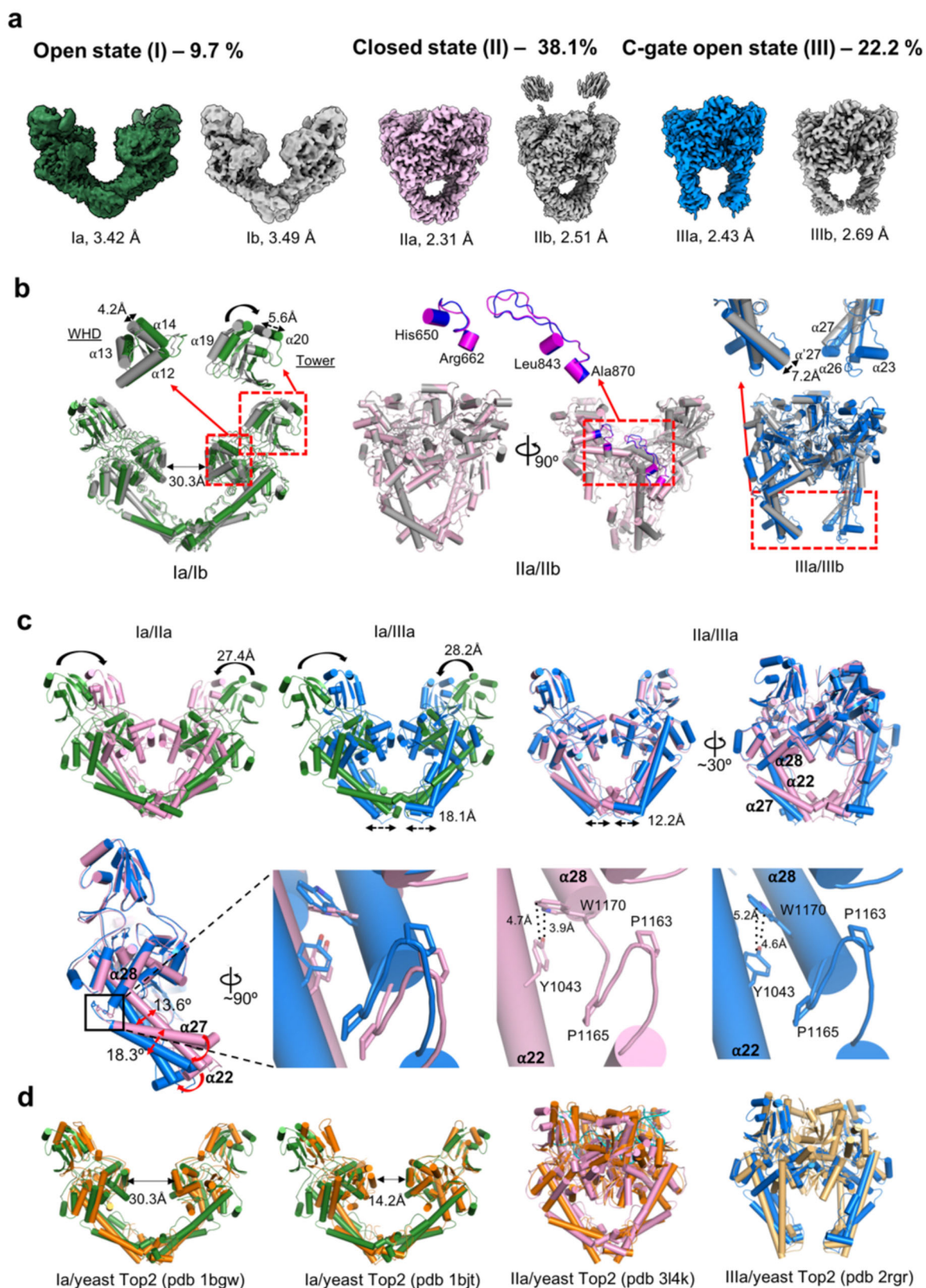
### Incompetence of *apo*-I for ligand binding

The results from the preceding section suggest that, even though the global conformation of *apo*-IIa is very similar to that of EDI-1, binding of DNA/inhibitor still induces small subdomain reorientations (Supplementary Movie 3: DNA-induced subdomain reorientation of *Asfv*-Top2), yet coupled with substantial catalytically relevant conformational changes locally. On the other hand, as shown in Fig. 4f, the three β-HPs and the catalytic Y800 in *apo*-Ia are farther away, relative to the corresponding moieties in *apo*-IIa, from the catalytically relevant positions in EDI-1, suggesting that it is less feasible for *apo*-I to bind the DNA substrate and undergo functionally relevant conformational changes. Taken together, our results suggest that it is advantageous for *apo*-II to coexist with *apo*-I through the catalytic selection process in order to be selected by the ligands, and to undergo further induced changes after ligand binding.

### Functional selection by redox regulation

The ATPase domain regulates the Top2 catalytic cycle by binding ATP to induce closure of the N-gate, followed by hydrolyzing ATP to stimulate cleavage and passage of DNA<sup>40,41,51,53,55,56,58,70</sup> (Fig. 1b), though the specific structural basis remains elusive. Here we report a different type of regulation by the ATPase domain of *Asfv*-Top2. Using X-ray crystallography, we first found that the ATPase domain of *Asfv*-Top2 seemed to coexist in two conformers in the MgAMP-PNP-bound crystal structure, and suspected that it could be a mixture of reduced and oxidized forms. Then we resolved the crystal structure of *Asfv*-Top2 ATPase domain complexed with MgAMP-PNP in the presence of the reducing agent β-mercaptoethanol (β-ME) (Fig. 5a, with density maps in Supplementary Fig. 12a). This structure showed unique features relative to the corresponding ATPase domain from *E. coli* and yeast Top2 (Supplementary Note 3 and Supplementary Fig. 13).

Next we address a new regulatory mechanism unique to *Asfv*-Top2. The crystal structure of *Asfv*-Top2 ATPase domain obtained from a non-reducing condition was solved at 1.14 Å resolution (Supplementary Note 3, with density maps in Supplementary Fig. 12). Structural analysis indicates that the structures from reducing and non-reducing conditions are without and with a C72-C138 disulfide bond, respectively (Fig. 5a, b). Interestingly, the disulfide bond formation involves a large movement of C72 to reach C138, along with relocation of H73 to pair with D137. Both residues and C138 are located at the solvent-exposed loops, in favor of the local motions. Additionally, this significant movement led to partial deformation of helix-α2 (Fig. 5b). The formation of disulfide bond between C72-C138 and the involvement of H73 are supported by mass spectrometry and NMR, respectively (Supplementary Fig. 14a, b).



Kinetic assays further indicated that the ATP hydrolysis activity was significantly dampened upon oxidation (Fig. 5c). Furthermore, under non-oxidizing condition, mutation of the residues involved in the disulfide bond formation, including H68A, C72A, H73A, and C138A, also led to different extent of inactivation, suggesting that these residues play additional roles in

the non-oxidizing environment. H68 and C72 appeared to be crucial in holding adenosine moiety of AMP-PNP in position and thus both alanine mutations significantly attenuated the ATP hydrolysis activity. C138 resides at the long extended loop (residues F<sub>125</sub>-G<sub>147</sub>), encompassing the conserved ATP-lid that completely encloses the bound MgAMP-PNP at the active site



**Fig. 2 | Structures of six conformers from *apo*-AsfvTop2.** **a** Cryo-EM density maps for the six conformers of the full-length *AsfvTop2*. The selected particle percentages of conformer I, II and III are labeled. The densities for the subdomains were clearly defined at a resolution of 2.31–3.49 Å, except for the ATPase domain. Sparse densities for ATPase of conformer IIb can be seen, which indicates that these domains were not cleaved in the process of obtaining structures, but were flexible instead. The TOPRIM subdomain is not modeled in the conformer I. **b** High resolution cryo-EM reconstructions of the *apo*-*AsfvTop2* cleavage core domain for the three states (I–III), with the two sub-conformers of each state superposed with each other. The distance between the Ca atoms of the Y744/Y744 from the two  $\alpha$ -helices 13 on the WHD subdomains of the two subunits is shown for Ia (Ia: 30.3 Å; Ib: 27.6 Å). The detailed

differences between sub-conformers are shown in insets. Annotation of the helices is based on the structure-based alignment (Supplementary Figs. 5, 6). **c** Upper panel: Superposed structures showing major conformational changes between conformers Ia and IIa (left); Ia and IIIa (center), and IIa and IIIa (right). The TOPRIM subdomain is omitted for clarity. Lower panel: The hinge connecting helix  $\alpha 27$  and  $\alpha 28$  contains two non-conserved proline residues. The residues and contacts that contribute to the structural differences are labeled. **d** Superposition of Ia, Ib, IIa, and IIIa with the comparable crystal structures from the yeast *Top2* cleavage core: pdb 1bgw (*apo*, TOPRIM omitted)<sup>40</sup>, 1bjt (*apo*, TOPRIM omitted)<sup>46</sup>, 314k (crossed-linked with dsDNA, closed state)<sup>64</sup>, and 2grg (complexed with dsDNA, closed state with C-gate open)<sup>48</sup>, respectively.

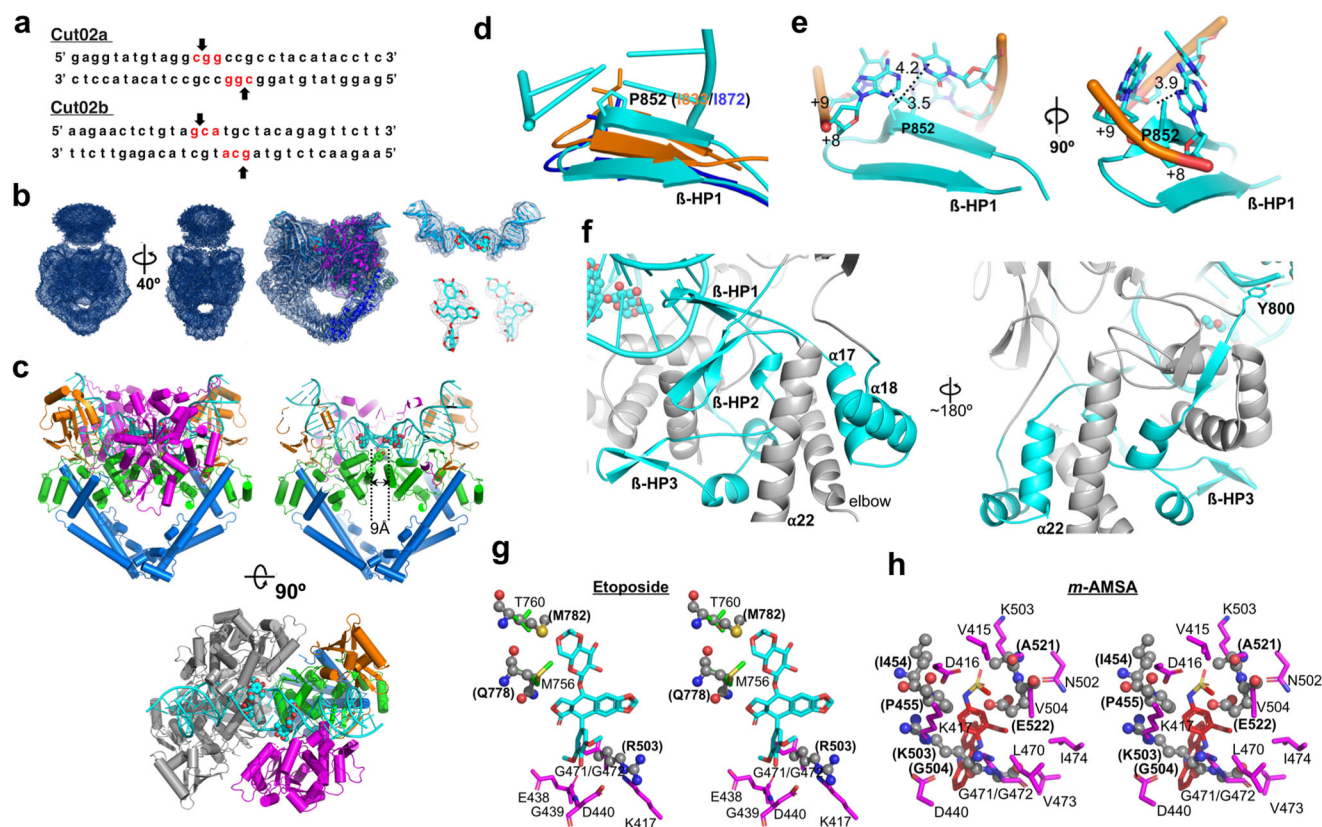


**Fig. 3 | Cryo-EM structure of *AsfvTop2*-DNA-drug complex showing unique DNA interactions and drug binding modes.** **a** The DNA sequences of the two G-DNA segments (Cut02a and Cut02b). The cleavage sites are indicated with arrows. **b** Left: The representative global cryo-EM density of the full-length complexes, *AsfvTop2* Cut02a/inhibitor (EDI-1, resolution 2.70 Å, contoured at 0.034  $\sigma$ ). Center: The global map fitted with the modeled cartoon structure, contoured at 0.198  $\sigma$ . Right: Maps of bound DNA and inhibitor molecules. **c** Left: The EDI-1 complex is shown in cartoon cylinders and colored based on the color scheme in Fig. 1a. Center/right: The structure is slabbed through to see the two  $\alpha$ -helices 13 clearly with their distance labeled. The DNA and inhibitor are colored in cyan with cartoon and sphere presentations, respectively. **d** Enlarged view of the overlaid  $\beta$ -

HP1 region (colored in cyan, residues 846–861). The conserved isoleucine in yeast (orange)/human (blue) *Top2s*<sup>64,66</sup> and *AsfvTop2* P852 (shown in stick) emanate towards DNA to different extents. **e** The intercalation of P852 and its distances (Å) to adjacent DNA bases are labeled. **f** Left: the spatial location of the  $\beta$ -HP1, adjacent to  $\beta$ -HP2 (residues 822–834) and  $\beta$ -HP3 (residues 1012–1025), and the elbow region. Right:  $\beta$ -HP1 is linked to the catalytic Y800 through  $\beta$ -HP3. The structural moieties mentioned are highlighted in cyan. **g, h** Structural superimposition between *AsfvTop2* and human *Top2* showing the differences in drug binding in stereo views. The corresponding human *Top2* residues (pdb 3qx3, etoposide bound<sup>66</sup>, pdb 4g0u, *m*-AMSA bound<sup>68</sup>) are shown in spheres and labeled in bold letters in parentheses.

(Fig. 5a, b, Supplementary Fig. 13b), therefore C138A mutation could affect the flexibility of the loop and subsequently the ATP hydrolysis. This effect appeared independent of the redox condition since the activity of C138A remained low in the oxidized form (Supplementary Fig. 14c). Thus, formation of the C72–C138 disulfide bond is most likely a naturally occurring way, in place of mutation, to enable the regulation of the ATPase activity and presumably the topoisomerase function. Importantly, this disulfide bond-mediated regulation of ATPase activity has not been shown in other *Top2* enzymes. Furthermore, we showed that C72A significantly affected DNA decatenation activity of the full-length *AsfvTop2* (Fig. 5d, Supplementary

Fig. 14d, e), which demonstrates that the oxidation-mediated ATPase inactivation shown in Fig. 5c can regulate the primary function of the *AsfvTop2*.

These structural and functional analyses further support that the conformational states of the ATPase domain are coupled to the conformational and functional states of the cleavage core. Although the full-length structure of *AsfvTop2* is not attainable due to conformational flexibility of the linker region that bridges two major functional domains, we have obtained a modeled structure based on the cryo-EM structure of the EDI-1 complex and the crystal structure of the ATPase



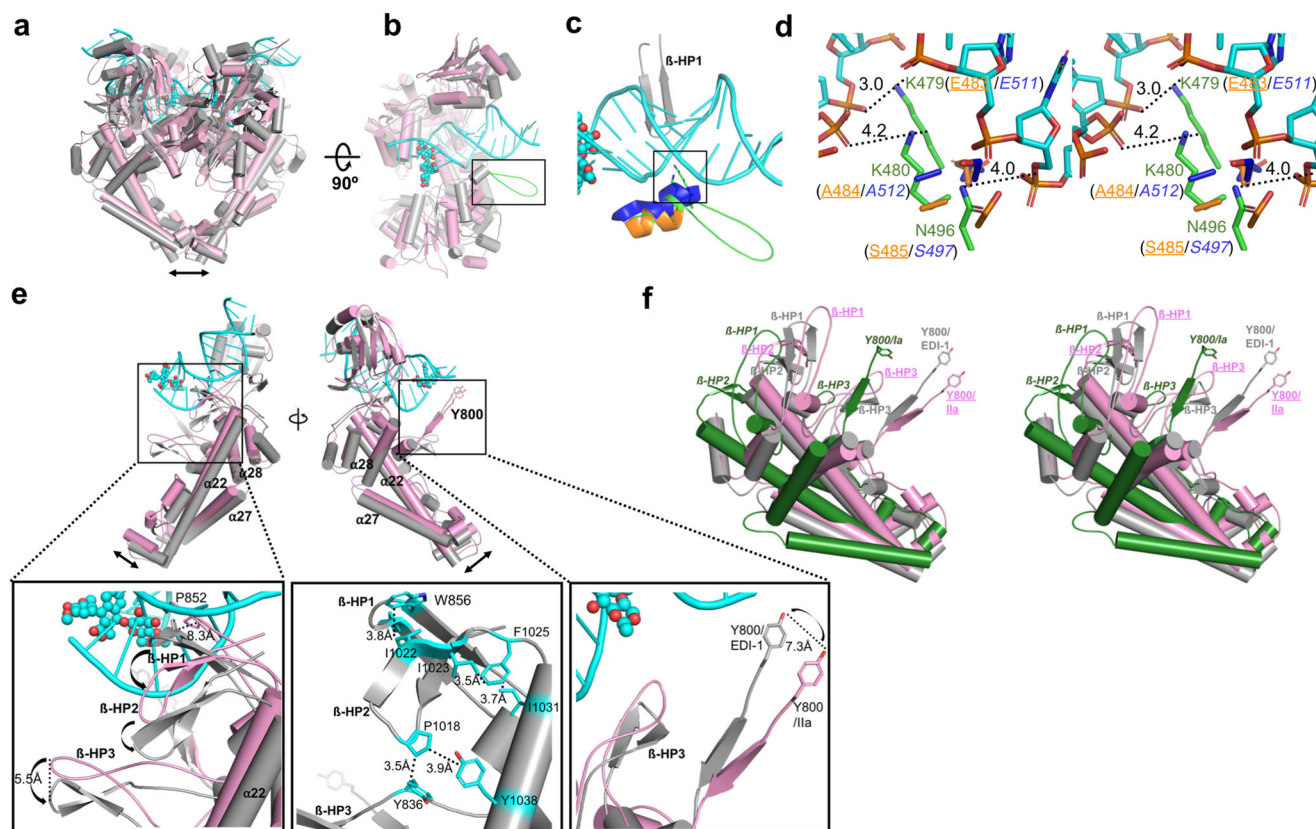


**Fig. 4 | Global and local conformational changes induced by DNA binding.** **a** The subdomain reorganization of *AsfvTop2* is illustrated by aligning EDI-1 (gray) with *apo*-IIa (pink). **b** Half model of **a**, with a 90° rotation around the *x*-axis. The black rectangle highlights the extended loop that appears upon DNA binding. **c** The extended loop (residues 481–493, colored in green) shown inside the black square in panel **b**. The corresponding region in yeast/human *Top2*<sup>64,66</sup> is colored in orange/blue, respectively. **d** The close-up stereo view of the specific interactions between *AsfvTop2* and DNA in the square box in (**c**). The interactions are governed by the K479 and K480 of *AsfvTop2*, which are replaced with Glu and Ala (residue numbers in parentheses), respectively, in yeast/human *Top2*. **e** Upper panels: A global view of

the local movements upon DNA binding with focus on the  $\beta$ -HP1 region (left) and the catalytic Y800 (right). Lower panels: The enlarged view of the squared regions in the upper panel. Left: The three  $\beta$ -HP loops from *apo*-IIa concurrently shift downward in the EDI-1 complex. Middle: The hydrophobic network that coordinates the concurrent movements of the three  $\beta$ -HPs and  $\alpha$ 22 in the EDI-1 complex. Right: Shifting of the catalytic Y800 toward DNA in the complex. **f** Stereo view for the spatial locations of the three  $\beta$ -HPs and Y800 in *apo*-Ia (colored in green with italic label), *apo*-IIa (colored in pink with underlined label), and the EDI-1 complex (gray).

domain, as described in Supplementary Note 4 and Supplementary Fig. 15.

Our result is in line with the redox-regulation of *AsfvPolX*<sup>71,72</sup> and *AsfvAP*<sup>73</sup>, which have been shown to exist in both reduced and oxidized forms involving C81–C86 and C16–C20, respectively. The oxidized form of *AsfvPolX* has been shown to be specific to GG mismatch in addition to the four Watson-Crick base pairs<sup>74</sup>, whereas the reduced form has higher fidelity<sup>75</sup>. The structural basis of the low fidelity of the oxidized *AsfvPolX* has been elucidated by NMR<sup>76</sup>. *AsfvPolX* and *AsfvAP*, along with a low-fidelity *Asfv* DNA ligase<sup>77</sup> are the key enzymes in the *Asfv* base excision repair system<sup>78,79</sup>. In line with the redox regulation of *AsfvPolX* and *AsfvAP*, formation of the disulfide bond by the cysteine pair (C72–C138) of *AsfvTop2* can lower the activity of the topoisomerase, thus also save the ATP consumption and slow down DNA replication and cell growth, all of which may favor survival of the virus in under oxidative stress. Taken together, we propose that the redox mediated conformational transition of *AsfvTop2* ATPase domain from reduced to oxidized state via the cysteine pair C72–C138 is a part of the functional selection, along with the redox regulations of *AsfvPolX* and *AsfvAP*, for the virus to adapt to the oxidizing environment of macrophage cytoplasm, analogous to catalytic selection in catalysis.

## Conclusion

As a conclusion, we quote a statement by D. E. Koshland from his 1994 review entitled “The Key-Lock Theory and the Induced Fit Theory”<sup>80</sup> with

relevant terms from recent literature inserted in parentheses: “A new theory (conformational selection<sup>3–5</sup>, or conformational selection followed by induced fit<sup>4,6,7</sup>) must explain all the existing facts that pertain to it at the time of its enunciation. Gradually the new theory becomes accepted and then acquires anomalies due to the new facts uncovered after its enunciation. That in turn generates a newer theory (catalytic selection<sup>8,9</sup>) which elicits new techniques (cryo-EM) to test it and its predictions. These new techniques then uncover facts which eventually require further new theories and so on. The new theories are built on components of the old principles.” In this study, the newest theory is the combination of the old components in order: (1) catalytic selection by the enzyme, (2) conformational selection by the substrates, and induced fit together, as illustrated in Fig. 5e. For signaling or other function, the first step should be replaced by “functional selection by the protein”. We propose that such a three-stage mechanism is universal in enzyme catalysis or protein-ligand recognitions, and expect that it will be demonstrated in more examples in the future.

## Methods

A brief summary is provided here. The functionally active full-length *AsfvTop2* was over-expressed and purified from the yeast protein expression system (Supplementary Fig. 7) for cryo-EM structure determination of *apo*-*AsfvTop2* and its DNA-inhibitor bound complexes (Supplementary Figs. 1–4). The functional studies performed included DNA decatenation, DNA relaxation, and cleavage assays (Fig. 5d, Supplementary Figs. 7, 8, 14).

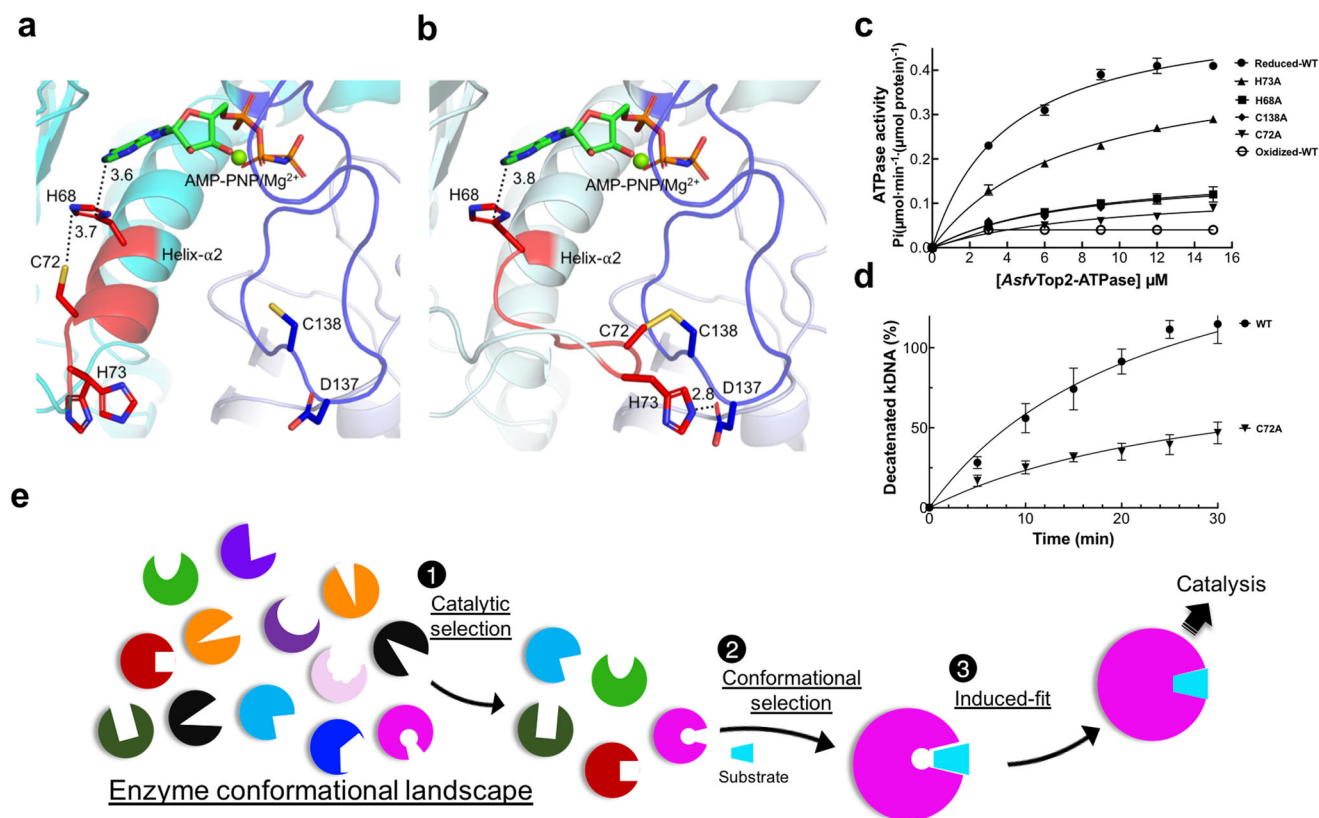


**Fig. 5 | A potential redox regulatory mechanism unique to *AsfvTop2*.** **a, b** The close-up view for the relative positions of MgAMP-PNP and the essential residues (C72, C138, H68, H73, and D137, all in stick presentation) involved in the potential regulatory mechanism. The reduced (**a**) and oxidized (**b**) forms are shown in cyan and pale cyan cartoon presentations, respectively. The disulfide bond between C72 and C138 is shown in brown stick. D137 and C138 are located at a long-extended surface loop (colored in blue) that harbors the active site residues interacting with the triphosphate group of the AMP-PNP. The segment E69-H73 that moves to form the disulfide bond is shown in red. **c** Analysis of ATP hydrolysis for the *AsfvTop2* ATPase domain in the presence of 1 mM ATP and varying concentrations of the enzyme. The y-axis shows the specific activity from each measurement. Raw data are provided in Supplementary Data 5. **d** C72A mutation of the full-length *AsfvTop2*

resulted in significant reduction of DNA decatenation activity in comparison to the wild type over different time points. Detailed conditions are described in Supplementary Fig. 13c, d. Raw data are provided in Supplementary Data 6. Each data point in panels c, d includes the mean  $\pm$  SE value from three independent reactions ( $n = 3$ ) from the same batch of sample. Similar assay methods for ATPase and decatenation activities have been used previously for other Top2 proteins<sup>35,83</sup>. **e** A graphical summary illustrating that the enzyme-substrate recognition is mediated by the joint application of the substrate binding theories in order: (1) catalytic selection, (2) conformational selection, and (3) induced fit. The catalytic selection should be replaced by functional selection when referring to other functions instead of catalysis.

The active *AsfvTop2* ATPase domain and its mutants were over-expressed and purified from *E. coli* for crystal structure determination (Supplementary Figs. 12, 13), redox studies, ATP hydrolysis activity assays (Figs. 5), 1D NMR, and mass spectrometry (Supplementary Fig. 14). The raw data for the functional and biophysical analyses are provided in Supplementary Data 1–6. A detailed explanation of all the procedures can be found in the Supplementary Methods section.

### Reporting summary

Further information on research design is available in the Nature Portfolio Reporting Summary linked to this article.

### Data availability

The coordinates and structure factors for *AsfvTop2* ATPase domain in the reduced and oxidized states have been deposited in the Worldwide Protein Data Bank (wwPDB) under the accession codes: 8JA2 and 8JA1. Cryo-EM maps and the corresponding coordinate files for the *apo* full length *AsfvTop2* have been deposited in the wwPDB under accession codes: 8J87, EMD-36062 (conformer Ia); 8J88, EMD-36063 (conformer Ib); 8J89, EMD-36064 (conformer IIa); 8J8A, EMD-36065 (conformer IIb); 8J8B, EMD-36066 (conformer IIIa); and 8J8C, EMD-36067 (conformer IIIb). Accession

codes for the complexes are: 8J9V, EMD-36116 (Cut02aDNA/etoposide-bound, EDI-1); 8J9W, EMD-36117 (Cut02bDNA/etoposide-bound, EDI-2); and 8J9X, EMD-36118 (Cut02aDNA/*m*-AMSA-bound, EDI-3). The 3.68 Å cryo-EM map of full-length DNA/etoposide/AMP-PNP-bound *AsfvTop2* can be accessed in the EMD-36473. The raw data for the functional and biophysical analyses are provided in Supplementary Data 1–6. The formal PDB validation reports of all deposited structures and maps are provided in Supplementary Data 7–18. The files of Supplementary Data 1, 3, 4, 6 have been stored in Figshare with <https://doi.org/10.6084/m9.figshare.25123829>.

Received: 18 December 2023; Accepted: 14 February 2024;  
Published online: 28 February 2024

### References

1. Fischer, E. Einfluss der configuration auf die wirkung der enzyme. *Ber. Dtsch. Chem. Ges.* **27**, 2985–1993 (1894).
2. Koshland, D. E. Application of a theory of enzyme specificity to protein synthesis. *Proc. Natl Acad. Sci. USA* **44**, 98–104 (1958).
3. Monod, J., Wyman, J. & Changeux, J. P. On the nature of allosteric transitions: a plausible model. *J. Mol. Biol.* **12**, 88–118 (1965).

4. Ma, B. & Nussinov, R. Enzyme dynamics point to stepwise conformational selection in catalysis. *Curr. Opin. Chem. Biol.* **14**, 652–659 (2010).
5. Weikl, T. R. & Paul, F. Conformational selection in protein binding and function. *Protein Sci.* **23**, 1508–1518 (2014).
6. Boehr, D. D., Nussinov, R. & Wright, P. E. The role of dynamic conformational ensembles in biomolecular recognition. *Nat. Chem. Biol.* **5**, 789–796 (2009).
7. Stiller, J. B. et al. Structure determination of high-energy states in a dynamic protein ensemble. *Nature* **603**, 528–535 (2022).
8. Henzler-Wildman, K. A. et al. Intrinsic motions along an enzymatic reaction trajectory. *Nature* **450**, 838–844 (2007).
9. Henzler-Wildman, K. & Kern, D. Dynamic personalities of proteins. *Nature* **450**, 964–972 (2007).
10. Austin, R. H., Beeson, K. W., Eisenstein, L., Frauenfelder, H. & Gunsalus, I. C. Dynamics of ligand binding to myoglobin. *Biochemistry* **14**, 5355–5373 (1975).
11. Bhabha, G. et al. A dynamic knockout reveals that conformational fluctuations influence the chemical step of enzyme catalysis. *Science* **332**, 234–238 (2011).
12. Whittier, S. K., Hengge, A. C. & Loria, J. P. Conformational motions regulate phosphoryl transfer in related protein tyrosine phosphatases. *Science* **341**, 899–903 (2013).
13. Kern, D. From structure to mechanism: skiing the energy landscape. *Nat. Methods* **18**, 435–436 (2021).
14. Nam, K. & Wolf-Watz, M. Protein dynamics: the future is bright and complicated! *Struct. Dyn.* **10**, 014301 (2023).
15. Petrovic, D., Risso, V. A., Kamerlin, S. C. L. & Sanchez-Ruiz, J. M. Conformational dynamics and enzyme evolution. *J. R. Soc. Interface* **15**, 20180330 (2018).
16. Ramanathan, A., Savol, A., Burger, V., Chennubhotla, C. S. & Agarwal, P. K. Protein conformational populations and functionally relevant substates. *Acc. Chem. Res.* **47**, 149–156 (2014).
17. Eisenmesser, E. Z. et al. Intrinsic dynamics of an enzyme underlies catalysis. *Nature* **438**, 117–121 (2005).
18. Sawaya, M. R., Pelletier, H., Kumar, A., Wilson, S. H. & Kraut, J. Crystal structure of rat DNA polymerase beta: evidence for a common polymerase mechanism. *Science* **264**, 1930–1935 (1994).
19. Liu, M. S. et al. Structural mechanism for the fidelity modulation of DNA polymerase lambda. *J. Am. Chem. Soc.* **138**, 2389–2398 (2016).
20. Moon, A. F. et al. Sustained active site rigidity during synthesis by human DNA polymerase mu. *Nat. Struct. Mol. Biol.* **21**, 253–260 (2014).
21. Delarue, M. et al. Crystal structures of a template-independent DNA polymerase: murine terminal deoxynucleotidyltransferase. *EMBO J.* **21**, 427–439 (2002).
22. Volkman, B. F., Lipson, D., Wemmer, D. E. & Kern, D. Two-state allosteric behavior in a single-domain signaling protein. *Science* **291**, 2429–2433 (2001).
23. Kerns, S. J. et al. The energy landscape of adenylate kinase during catalysis. *Nat. Struct. Mol. Biol.* **22**, 124–131 (2015).
24. Murata, K. & Wolf, M. Cryo-electron microscopy for structural analysis of dynamic biological macromolecules. *Biochim Biophys. Acta Gen. Subj.* **1862**, 324–334 (2018).
25. Tsai, M. D., Wu, W. J. & Ho, M. C. Enzymology and dynamics by cryogenic electron microscopy. *Annu Rev. Biophys.* **51**, 19–38 (2022).
26. Dashti, A. et al. Trajectories of the ribosome as a Brownian nanomachine. *Proc. Natl. Acad. Sci. USA* **111**, 17492–17497 (2014).
27. Frank, J. & Ourmazd, A. Continuous changes in structure mapped by manifold embedding of single-particle data in cryo-EM. *Methods* **100**, 61–67 (2016).
28. Roh, S. H. et al. Subunit conformational variation within individual GroEL oligomers resolved by Cryo-EM. *Proc. Natl. Acad. Sci. USA* **114**, 8259–8264 (2017).
29. Haselbach, D. et al. Structure and conformational dynamics of the human spliceosomal B(act) complex. *Cell* **172**, 454–464 e411 (2018).
30. Murphy, B. J. et al. Rotary substates of mitochondrial ATP synthase reveal the basis of flexible F(1)-F(o) coupling. *Science* **364**, eaaw9128 (2019).
31. Schulz, F., Abergel, C. & Woyke, T. Giant virus biology and diversity in the era of genome-resolved metagenomics. *Nat. Rev. Microbiol.* **20**, 721–736 (2022).
32. Sanchez-Cordon, P. J., Montoya, M., Reis, A. L. & Dixon, L. K. African swine fever: a re-emerging viral disease threatening the global pig industry. *Vet. J.* **233**, 41–48 (2018).
33. Karger, A. et al. An update on African swine fever virology. *Viruses* **11**, 864 (2019).
34. Coelho, J., Martins, C., Ferreira, F. & Leitao, A. African swine fever virus ORF P1192R codes for a functional type II DNA topoisomerase. *Virology* **474**, 82–93 (2015).
35. Coelho, J., Ferreira, F., Martins, C. & Leitao, A. Functional characterization and inhibition of the type II DNA topoisomerase coded by African swine fever virus. *Virology* **493**, 209–216 (2016).
36. Freitas, F. B., Frouco, G., Martins, C., Leitao, A. & Ferreira, F. In vitro inhibition of African swine fever virus-topoisomerase II disrupts viral replication. *Antivir. Res.* **134**, 34–41 (2016).
37. Baylis, S. A., Dixon, L. K., Vydellingum, S. & Smith, G. L. African swine fever virus encodes a gene with extensive homology to type II DNA topoisomerases. *J. Mol. Biol.* **228**, 1003–1010 (1992).
38. Coelho, J. & Leitao, A. The African swine fever virus (ASFV) topoisomerase II as a target for viral prevention and control. *Vaccines (Basel)* **8**, 312 (2020).
39. Zhu, Z. & Meng, G. ASFVdb: an integrative resource for genomic and proteomic analyses of African swine fever virus. *Database (Oxf.)* **2020**, baaa023 (2020).
40. Berger, J. M. & Osheroff, N. Structure and mechanism of eukaryotic type IIA topoisomerases. in *DNA Topoisomerases and Cancer* (ed Pommier, Y.) 87–101 (Springer, 2012).
41. Chen, S. H., Chan, N. L. & Hsieh, T. S. New mechanistic and functional insights into DNA topoisomerases. *Annu Rev. Biochem.* **82**, 139–170 (2013).
42. Pommier, Y., Sun, Y., Huang, S. N. & Nitiss, J. L. Roles of eukaryotic topoisomerases in transcription, replication and genomic stability. *Nat. Rev. Mol. Cell Biol.* **17**, 703–721 (2016).
43. Sutormin, D. A. et al. Diversity and functions of type II topoisomerases. *Acta Nat.* **13**, 59–75 (2021).
44. McKie, S. J., Neuman, K. C. & Maxwell, A. DNA topoisomerases: advances in understanding of cellular roles and multi-protein complexes via structure-function analysis. *Bioessays* **43**, e2000286 (2021).
45. Berger, J. M., Gamblin, S. J., Harrison, S. C. & Wang, J. C. Structure and mechanism of DNA topoisomerase II. *Nature* **379**, 225–232 (1996).
46. Fass, D., Bogden, C. E. & Berger, J. M. Quaternary changes in topoisomerase II may direct orthogonal movement of two DNA strands. *Nat. Struct. Biol.* **6**, 322–326 (1999).
47. Corbett, K. D., Schoeffler, A. J., Thomsen, N. D. & Berger, J. M. The structural basis for substrate specificity in DNA topoisomerase IV. *J. Mol. Biol.* **351**, 545–561 (2005).
48. Dong, K. C. & Berger, J. M. Structural basis for gate-DNA recognition and bending by type IIA topoisomerases. *Nature* **450**, 1201–1205 (2007).
49. Schmidt, B. H., Osheroff, N. & Berger, J. M. Structure of a topoisomerase II-DNA-nucleotide complex reveals a new control mechanism for ATPase activity. *Nat. Struct. Mol. Biol.* **19**, 1147–1154 (2012).
50. Wendorff, T. J., Schmidt, B. H., Heslop, P., Austin, C. A. & Berger, J. M. The structure of DNA-bound human topoisomerase II alpha:



- conformational mechanisms for coordinating inter-subunit interactions with DNA cleavage. *J. Mol. Biol.* **424**, 109–124 (2012).
51. Laponogov, I. et al. Structure of an ‘open’ clamp type II topoisomerase-DNA complex provides a mechanism for DNA capture and transport. *Nucleic Acids Res.* **41**, 9911–9923 (2013).
  52. Wang, Y. et al. Structure of African swine fever virus and associated molecular mechanisms underlying infection and immunosuppression: a review. *Front. Immunol.* **12**, 715582 (2021).
  53. Brino, L. et al. Dimerization of Escherichia coli DNA-gyrase B provides a structural mechanism for activating the ATPase catalytic center. *J. Biol. Chem.* **275**, 9468–9475 (2000).
  54. Hu, T., Sage, H. & Hsieh, T. S. ATPase domain of eukaryotic DNA topoisomerase II. Inhibition of ATPase activity by the anti-cancer drug bisdioxopiperazine and ATP/ADP-induced dimerization. *J. Biol. Chem.* **277**, 5944–5951 (2002).
  55. Classen, S., Olland, S. & Berger, J. M. Structure of the topoisomerase II ATPase region and its mechanism of inhibition by the chemotherapeutic agent ICRF-187. *Proc. Natl. Acad. Sci. USA* **100**, 10629–10634 (2003).
  56. Bates, A. D. & Maxwell, A. The role of ATP in the reactions of type II DNA topoisomerases. *Biochem Soc. Trans.* **38**, 438–442 (2010).
  57. Blower, T. R. et al. A complex suite of loci and elements in eukaryotic type II topoisomerases determine selective sensitivity to distinct poisoning agents. *Nucleic Acids Res.* **47**, 8163–8179 (2019).
  58. Laponogov, I. et al. Trapping of the transport-segment DNA by the ATPase domains of a type II topoisomerase. *Nat. Commun.* **9**, 2579 (2018).
  59. Chen, S. F. et al. Structural insights into the gating of DNA passage by the topoisomerase II DNA-gate. *Nat. Commun.* **9**, 3085 (2018).
  60. Zhao, Y. et al. Cryo-EM structures of African swine fever virus topoisomerase. *mBio* **14**, e0122823 (2023).
  61. Ho, B. K., Coutsias, E. A., Seok, C. & Dill, K. A. The flexibility in the proline ring couples to the protein backbone. *Protein Sci.* **14**, 1011–1018 (2005).
  62. Wang, J. C. Moving one DNA double helix through another by a type II DNA topoisomerase: the story of a simple molecular machine. *Q Rev. Biophys.* **31**, 107–144 (1998).
  63. Soczek, K. M., Grant, T., Rosenthal, P. B. & Mondragon, A. CryoEM structures of open dimers of gyrase A in complex with DNA illuminate mechanism of strand passage. *Elife* **7**, e41215 (2018).
  64. Schmidt, B. H., Burgin, A. B., Deweese, J. E., Osheroff, N. & Berger, J. M. A novel and unified two-metal mechanism for DNA cleavage by type II and IA topoisomerases. *Nature* **465**, 641–644 (2010).
  65. Pommier, Y., Leo, E., Zhang, H. & Marchand, C. DNA topoisomerases and their poisoning by anticancer and antibacterial drugs. *Chem. Biol.* **17**, 421–433 (2010).
  66. Wu, C. C. et al. Structural basis of type II topoisomerase inhibition by the anticancer drug etoposide. *Science* **333**, 459–462 (2011).
  67. Lee, I., Dong, K. C. & Berger, J. M. The role of DNA bending in type IIA topoisomerase function. *Nucleic Acids Res.* **41**, 5444–5456 (2013).
  68. Wu, C. C., Li, Y. C., Wang, Y. R., Li, T. K. & Chan, N. L. On the structural basis and design guidelines for type II topoisomerase-targeting anticancer drugs. *Nucleic Acids Res.* **41**, 10630–10640 (2013).
  69. Vanden Broeck, A. et al. Structural basis for allosteric regulation of Human Topoisomerase IIalpha. *Nat. Commun.* **12**, 2962 (2021).
  70. Baird, C. L., Harkins, T. T., Morris, S. K. & Lindsley, J. E. Topoisomerase II drives DNA transport by hydrolyzing one ATP. *Proc. Natl. Acad. Sci. USA* **96**, 13685–13690 (1999).
  71. Maciejewski, M. W. et al. Solution structure of a viral DNA repair polymerase. *Nat. Struct. Biol.* **8**, 936–941 (2001).
  72. Showalter, A. K., Byeon, I. J., Su, M. I. & Tsai, M. D. Solution structure of a viral DNA polymerase X and evidence for a mutagenic function. *Nat. Struct. Biol.* **8**, 942–946 (2001).
  73. Chen, Y. et al. A unique DNA-binding mode of African swine fever virus AP endonuclease. *Cell Discov.* **6**, 13 (2020).
  74. Showalter, A. K. & Tsai, M. D. A DNA polymerase with specificity for five base pairs. *J. Am. Chem. Soc.* **123**, 1776–1777 (2001).
  75. Voehler, M. W., Eoff, R. L., McDonald, W. H., Guengerich, F. P. & Stone, M. P. Modulation of the structure, catalytic activity, and fidelity of African swine fever virus DNA polymerase X by a reversible disulfide switch. *J. Biol. Chem.* **284**, 18434–18444 (2009).
  76. Wu, W. J. et al. How a low-fidelity DNA polymerase chooses non-Watson-Crick from Watson-Crick incorporation. *J. Am. Chem. Soc.* **136**, 4927–4937 (2014).
  77. Lamarche, B. J., Showalter, A. K. & Tsai, M. D. An error-prone viral DNA ligase. *Biochemistry* **44**, 8408–8417 (2005).
  78. Showalter, A. K. et al. Mechanistic comparison of high-fidelity and error-prone DNA polymerases and ligases involved in DNA repair. *Chem. Rev.* **106**, 340–360 (2006).
  79. Wang, G., Xie, M., Wu, W. & Chen, Z. Structures and functional diversities of ASFV proteins. *Viruses* **13**, 2124 (2021).
  80. Daniel, E. & Koshland, J. The key-lock theory and the induced fit theory. *Angew. Chem. Int. Ed. Engl.* **33**, 2375–2378 (1994).
  81. Baek, M. et al. Accurate prediction of protein structures and interactions using a three-track neural network. *Science* **373**, 871–876 (2021).
  82. Afonine, P. V. et al. Real-space refinement in PHENIX for cryo-EM and crystallography. *Acta Crystallogr D Struct. Biol.* **74**, 531–544 (2018).
  83. Ling, E. M. et al. A comprehensive structural analysis of the ATPase domain of human DNA topoisomerase II beta bound to AMPNP, ADP, and the bisdioxopiperazine, ICRF193. *Structure* **30**, 1129–1145 e1123 (2022).

## Acknowledgements

The authors thank Dr. Alexandre Leitão for kindly providing the original *AsfvTop2* protein expression plasmid, and Dr. Nei-Li Chan and Dr. Lars-Oliver Essen for the comments during manuscript preparation. The work was supported by Academia Sinica (AS-KPQ-109-TPP2) and Taiwan Cryo-EM Consortium funded by National Council of Science and Technology, grant no. NSTC 112-2740-B-006-001. Cryo-EM experiments were performed at the Academia Sinica Cryo-EM Facility, which is supported by Academia Sinica (AS-CFII-108-110) and Taiwan Protein Project (AS-KPQ-109-TPP2). The cryo-EM data were processed at the Academia Sinica Grid-computing Center supported by Academia Sinica. The X-ray crystallography data were collected at the Taiwan Photo Source (TPS) beamline 05 A, National Synchrotron Radiation Research Center (NSRRC), Taiwan. NMR data were collected at the Academia Sinica High Field Nuclear Magnetic Resonance Center (Grant No. AS-CFII-108-112). We thank Dr. Shu-Yu Lin for the support on the Mass spectrometry experiments conducted at the Proteomics Mass Spectrometry Common Facility, Institute of Biological Chemistry, Academia Sinica.

## Author contributions

C.-W.C. and M.-D.T. conceived and designed the research and wrote the paper. S.-C.W. characterized *AsfvTop2* preferential DNA sequences and designed experiments for protein expression, purification and activity assays. C.-W.C. and C.-H.W. performed cryo-EM experiments. C.-W.C., A.H.P., and Y.-K.C. performed X-ray crystallography experiments. W.-J.W. performed NMR experiments. C.-H.Y. and all other authors analyzed data.



### Competing interests

The authors declare no competing interests.

### Additional information

**Supplementary information** The online version contains supplementary material available at

<https://doi.org/10.1038/s42004-024-01129-y>.

**Correspondence** and requests for materials should be addressed to Ming-Daw Tsai.

**Peer review information** *Communications chemistry* thanks the anonymous reviewers for their contribution to the peer review of this work. A peer review file is available.

**Reprints and permissions information** is available at <http://www.nature.com/reprints>

**Publisher's note** Springer Nature remains neutral with regard to jurisdictional claims in published maps and institutional affiliations.

**Open Access** This article is licensed under a Creative Commons Attribution 4.0 International License, which permits use, sharing, adaptation, distribution and reproduction in any medium or format, as long as you give appropriate credit to the original author(s) and the source, provide a link to the Creative Commons licence, and indicate if changes were made. The images or other third party material in this article are included in the article's Creative Commons licence, unless indicated otherwise in a credit line to the material. If material is not included in the article's Creative Commons licence and your intended use is not permitted by statutory regulation or exceeds the permitted use, you will need to obtain permission directly from the copyright holder. To view a copy of this licence, visit <http://creativecommons.org/licenses/by/4.0/>.

© The Author(s) 2024